Research paper

Numerical and experimental benchmarking of the dynamic response of SiC and TZM specimens in the MultiMat experiment

Marcus Portelli[a,*], Alessandro Bertarelli[b], Federico Carra[b], Michele Pasquali[b], Nicholas Sammut[c], Pierluigi Mollicone[c]

[a] *University of Malta, Malta and CERN, Geneva, Switzerland*
[b] *CERN, Geneva, Switzerland*
[c] *University of Malta, Malta*

ABSTRACT

The MultiMat experiment was successfully conducted at CERN's HiRadMat facility, aiming to test novel high-performance materials for use in beam intercepting devices, allowing the derivation and validation of material constitutive models. This article provides an analysis of results for two materials tested in the experiment, namely Silicon Carbide and Titanium Zirconium Molybdenum, with the aim of benchmarking the material constitutive models currently available in literature with experimental results. The material models were implemented in numerical simulations, successfully modelling dynamic longitudinal and flexural phenomena. The article further studies the modelling of the complex boundary conditions present in the experiment, the internal damping characteristics of the materials, and the failure of certain specimens. The strength and failure models proved adequate to model a number of experimental scenarios tested, but require further study to describe the material behaviour at the high strain rates and temperatures induced by accidental particle beam impacts. A post-irradiation examination of the tested specimens was also performed to study the nature of failure in the specimens, and is to be coupled with quasi-static and high strain rate tests for both materials, allowing for the validation of the currently available models and the description of material behaviour across a wide range of strain rates and temperatures.

1. Introduction

In the upcoming high luminosity upgrade of the LHC (HL-LHC) (Apollinari et al., 2017), the energy stored in the circulating beams will increase from 360 to 680 MJ, while for the proposed Future Circular Collider (FCC) (Benedikt and Zimmerman, 2016) the beam energy is projected to reach up to 8500 MJ. This increase in beam energy brings the need for high-performing components, especially those in risk of accidental beam impacts, such as collimators and other beam intercepting devices (Carra et al., 2014). In such cases, for the HL-LHC, accidental impacts due to asynchronous beam dumps or injection errors may result in thermal loads exceeding energy densities of 10 kJ/cm^3 on the collimator jaws (Bertarelli, 2016), resulting in intense pressure waves propagating through the material, risking plasticity, fracture, and spallation of material, as well as melting and vaporization of the impacted region (Bertarelli et al., 2013).

With this in mind, the materials utilised for such components and exposed to such extreme conditions require extensive experimental

testing and validation in order to derive the constitutive models required to numerically simulate high energy particle beam impacts. Such tests are conducted in CERN's HiRadMat facility (Efthymiopoulos et al., 2011). Full-scale collimator jaws have been tested in the facility (Carra et al., 2014; Bertarelli et al., 2006; Cauchi et al., 2014), while the HRMT-14 experiment, performed in 2012 (Bertarelli et al., 2012), tested specimens with simple geometries in order to benchmark numerical results obtained through numerical analyses performed with codes such as ANSYS (ANSYS, Inc. 2013) and Autodyn (ANSYS, Inc. 2013). In October 2017, the HRMT-36 "MultiMat" experiment (Carra et al., 2017; Pasquali et al., 2019) was conducted at the HiRadMat facility. This experiment built on the experience gathered in previous experiments (Bertarelli et al., 2012; Bertarelli et al., 2013) and aimed to offer a reusable platform to test recently developed high-performance materials for beam intercepting devices (Quaranta, 2017; Bertarelli et al., 2014) impacted by particle beams with energy densities close to HL-LHC levels.

In this work, material constitutive models implemented in implicit

---

thermo-mechanical numerical simulations performed in ANSYS Workbench are benchmarked with experimental results from the MultiMat experiment. The work focuses on two materials tested in the experiment, namely Silicon Carbide and Titanium Zirconium Molybdenum, and considers longitudinal and flexural dynamic phenomena provoked by the particle beam impacts in the experiment. For both materials, one or more specimens fractured during the experiment.

The constitutive models initially adopted in numerical analyses consisted of temperature-dependent thermo-mechanical properties independent of strain rate, with the main goal of the study being to verify and extend the adopted constitutive models through the benchmarking with experimental data. The material models adopted from literature were deemed suitable to model the various phenomena and conditions tested in the experiment, with additional material testing at high strain rates projected to further bolster the models to allow the simulation of complex, high energy phenomena. The study further investigates the effects of boundary conditions on the flexural response, material damping in the experimental signal and its application in numerical analyses, as well as failure of the specimens and its simulation in the implicit numerical code – paving the way for more complex analyses on non-linear, anisotropic materials tested in the MultiMat experiment.

2. The MultiMat experiment

2.1. Experimental layout and instrumentation

As can be seen in Fig. 1, the test bench hosted 16 target stations, each having a total length of 1 m. The stations were mounted on a rotatable barrel, with each station hosting a number of material specimens in series, each in the form of a slender bar with lengths of 120 or 247 mm, and with cross-sections varying from 8×8 to 12×11.5 mm^2. The setup utilised an actuation system which allowed vertical and horizontal adjustment of specimens via stepper motors, as well as rotation achieved via a Geneva mechanism, allowing each target station to be brought into shooting position to be impacted by the incoming beam. 79 specimens were set up and 17 different materials were tested. The specimens were extensively equipped with strain gauges and thermal probes, along with remote instrumentation including a Laser Doppler Vibrometer (LDV) and a radiation-hard high-definition camera (Carra et al., 2017).

In the experimental setup, the specimens were placed on graphitic elastic supports at the two extremities and kept in contact with an upper support (at both extremities) via a preloaded compression applied on the spring. The steel springs had an original length of 14 mm and were compressed to 9 mm, for a preload of 13.57 N (given a stiffness of 2.7144 N/mm). Modal analyses performed prior to the experiment indicated that the system was close to a system being simply-supported at each end (Carra et al., 2017) and therefore, with this in mind, initial structural analyses performed in this study considered this scenario, modelled by restricting the bottom edges of the two samples' extremities from moving in the vertical direction. As will be discussed later, experimental results indicate that in some cases the beam impact resulted in specimens losing contact with the support, causing a change in boundary conditions. The specimens were extensively equipped with longitudinal strain gauges on the bottom face, with up to a maximum of 5 strain gauges on the most loaded specimens. A schematic showing the face denomination with respect to the adopted coordinate system, along with the typical position of longitudinal and transverse strain gauges and temperature probes, can also be seen in Fig. 1.
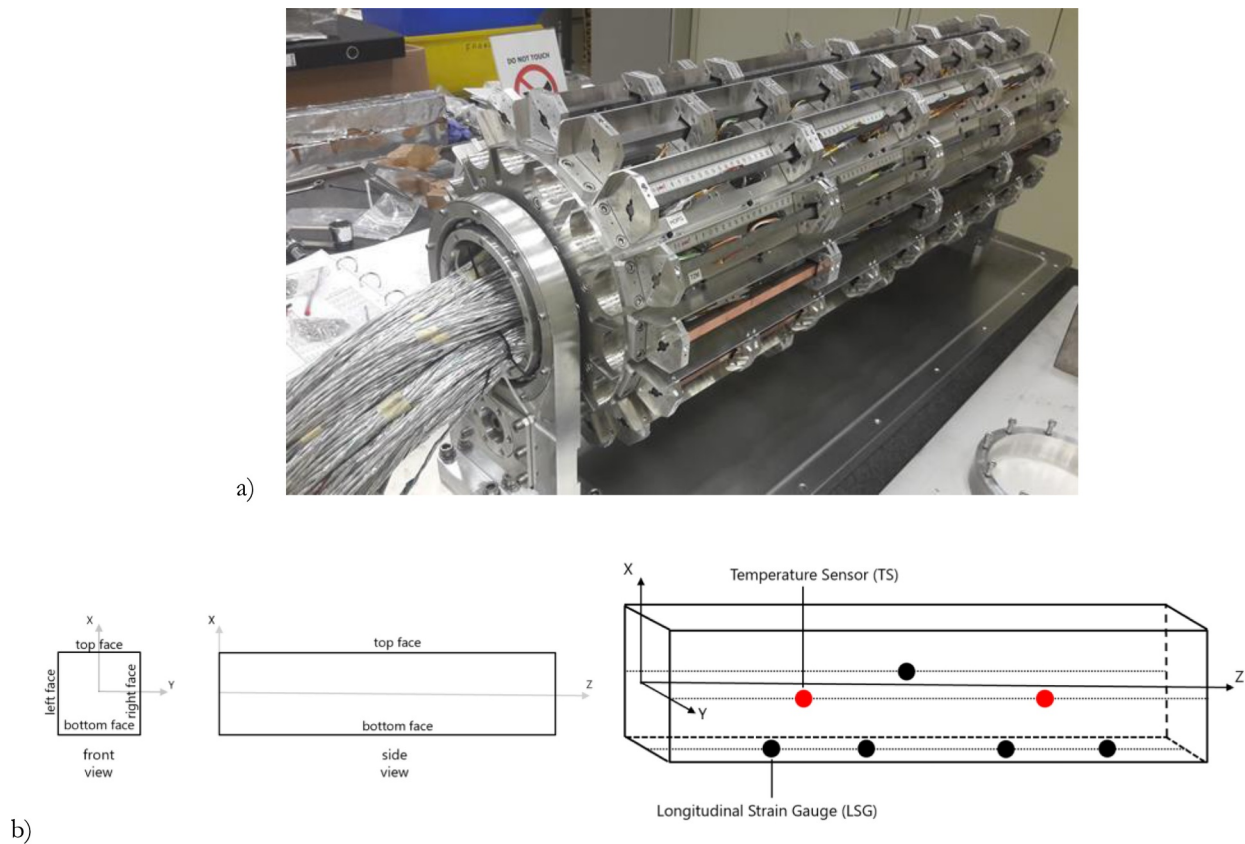

Fig. 1. Rotatable barrel with Geneva mechanism and mounted target stations in the HRMT-36 "MultiMat" experiment test bench (a), front/side view of specimens with face designation ((b), left) and typical position of longitudinal strain gauges (black) and temperature sensors (red) on the specimens ((b), right). (For interpretation of the references to colour in this figure legend, the reader is referred to the web version of this article.)

2.2. Materials tested in the MultiMat experiment

Several materials were tested in the MultiMat experiment. These can be grouped in six categories, mainly pure carbon materials, metal carbide – graphite composites (Bertarelli et al., 2014, 2015), titanium alloys, copper – diamond (Bertarelli et al., 2011), silicon carbide, and heavy alloys. Some of the carbon-based specimens were coated with copper, molybdenum or TiN thin films. A wide range of scenarios were tested, with pulse intensity ranging from 1 to 288 bunches (with a typical bunch intensity of 1.3×10^{11} protons) and nominal beam RMS sizes of 0.25×0.25, 0.5×0.5 and 2×2 mm^2. Three different types of impact were tested, namely axially centred impacts, offset impacts, and grazing impacts (where a coating was present). This study focuses on the first two types of impacts, with the former resulting in a longitudinal response, and the latter provoking an additional flexural response. Such impact scenarios result in the generation of different signals of interest, having distinct timescales which can be easily detected and decoupled, namely the signal rise time, related to the pulse duration, which is in the order of 10 μs, following which a longitudinal wave with a distinct trapezoidal shape is generated, with a period in the order of 100 μs. When the impact has a transverse offset across the specimen's cross section, flexural oscillations are also excited, having a period in the order of 1 ms (Bertarelli, 2016).

A large amount of data was gathered from the experiment, requiring post-processing and comparison with numerical simulation results. This paper focuses on the results for two materials, Silicon Carbide (SiC) and Titanium Zirconium Molybdenum (TZM), two materials which, as detailed, exhibited failure during the experiment. For both materials considered, the setup consisted of a station housing four specimens in series, each having dimensions of $10 \times 10 \times 247$ mm^3, with no coatings.

The SiC grade tested was manufactured by chemical vapour deposition (CVD) by Microcertec SAS (Microcertec, 2019). A linear elastic model was used for SiC, utilising temperature-dependent material properties supplied by the manufacturer.

The stress-relieved TZM grade tested was developed by Plansee (Plansee, 2019), and is composed of 0.4–0.55% Titanium, 0.06–0.12% Zirconium and Molybdenum balance. The manufacturing process to prepare the samples included a combination of pressing, sintering and forming before further heat treatment. For this material, only the coefficient of thermal expansion, specific heat capacity and thermal conductivity were available as temperature-dependent properties from the manufacturer's specification sheet. Therefore, elastic properties and a bilinear kinematic hardening constitutive model was adopted from literature (Shinno et al., 1988), with the tangent modulus (E_t) calculated by taking into consideration the provided elongation at failure (ε_f), tensile strength (TS), yield strength (σ_y) and Young's Modulus (E) by:

$$E_t = \frac{TS - \sigma_y}{\varepsilon_f - \frac{\sigma_y}{E}}$$

(1)

The temperature-dependent material properties adopted for the two materials can be seen in Fig. 2. The bilinear kinematic hardening parameters and tensile strength values adopted for TZM are shown in Table 1 along with the SiC flexural strength values provided by the manufacturer.

2.3. Beam parameters

In the experiment, each station was subject to a number of particle beam impacts with varying levels of deposited energy and beam position, including central, offset and grazing shots. In this study, two shots were considered for each material, one with a vertical offset and having caused no visible damage, and one which resulted in the failure of one or more specimens in the target station.

For the first scenario, a vertical beam offset (i.e. in the X-direction, with reference to the coordinate system introduced in Fig. 1) was considered for both materials in order to allow the study of both longitudinal and flexural effects. For the SiC line, the shot considered (shot 1) consisted of a 300 ns pulse with 12 bunches with a total intensity of 1.4×10^{12} protons, 0.5 mm beam sigma, and a vertical offset of 0.5 mm. For TZM, a 600 ns shot with 24 bunches with a total intensity of 2.64×10^{12} protons, 2 mm sigma, and a vertical offset of -2 mm was initially considered (shot 2).

In addition to these beam pulses which caused no visible damage to the samples, the shots resulting in the failure of the specimens were also considered in the last section of the study, detailing the failure scenario. All the shots considered in the study are summarised in Table 2. Note that shot 1 and shot 2 refer to the SiC and TZM shots respectively defined in the previous paragraph, whilst shot 1F and 2F refer to the shots causing failure in each respective material.

Additionally, it is important to note that shot 2F is the last of a series of three shots with increasing bunch intensity, and chronologically took place before shot 2. In fact, the effects of the failure caused by shot 2F can be observed in results probed from the failed specimen in shot 2. Given that each shots impinges all of the four specimens in the target station, following the failure of the second specimen, the specimens were still affected normally by subsequent shots (including shot 2). It is also interesting to note that shot 1F resulted in a relatively large amount of energy and peak energy deposited in the SiC specimens, when compared to shot 1. For TZM, shot 2F can be seen to have a lower total energy but a significantly higher peak compared to shot 2.

3. Analytical modelling of thermally induced stress waves

Particle beams interacting with matter cause part of their energy to be transferred to the material, under the form of a heat deposition, with a consequent sudden increase in temperature of the impacted material. Depending on the power density deposited, different effects may result from such interaction. Beam losses in particle accelerators result in a continuous energy deposition, which can last from a few seconds up to hours. In accidental beam impacts, the energy deposition time is in the order of nano to microseconds, resulting in a dynamic response of the impacted structure (Bertarelli, 2016). The topic of the dynamic response of slender rods subject to an almost instantaneous temperature increase is thus of particular interest for high energy particle physics applications, given the slender nature of many beam intercepting devices. As detailed, the MultiMat experiment was designed to analyse such a response, with the geometry of the samples chosen to decouple as much as possible the different phenomena occurring during the impact: as already stated, this study focuses on dynamic longitudinal and flexural phenomena.

3.1. Longitudinal phenomena

Analytical solutions for the longitudinal response of slender rods under such conditions have been proposed by Bargmann (1973), Sievers (1974). Bertarelli et al. (2008) have proposed solutions on both longitudinal and flexural responses. The analytical solutions simplify the setup by assuming a constant energy deposition over the longitudinal length of the rod and a Gaussian distribution across the cross-section, as well as neglecting material inertia in the radial direction.

The effect of a non-constant energy deposition over the longitudinal coordinate of the rod was discussed by Carra (2017), who described how this can result in longitudinal waves originating from the two extremities of the specimen having varying amplitudes based on the distribution of energy along the length. The effect of radial inertia on the longitudinal response was further studied by the author (Portelli et al., 2018), based on considerations made by Graff (1991), indicating that phenomena related to radial inertia, such as wave dispersion and Poisson ratio effects, also have a non-negligible effect on
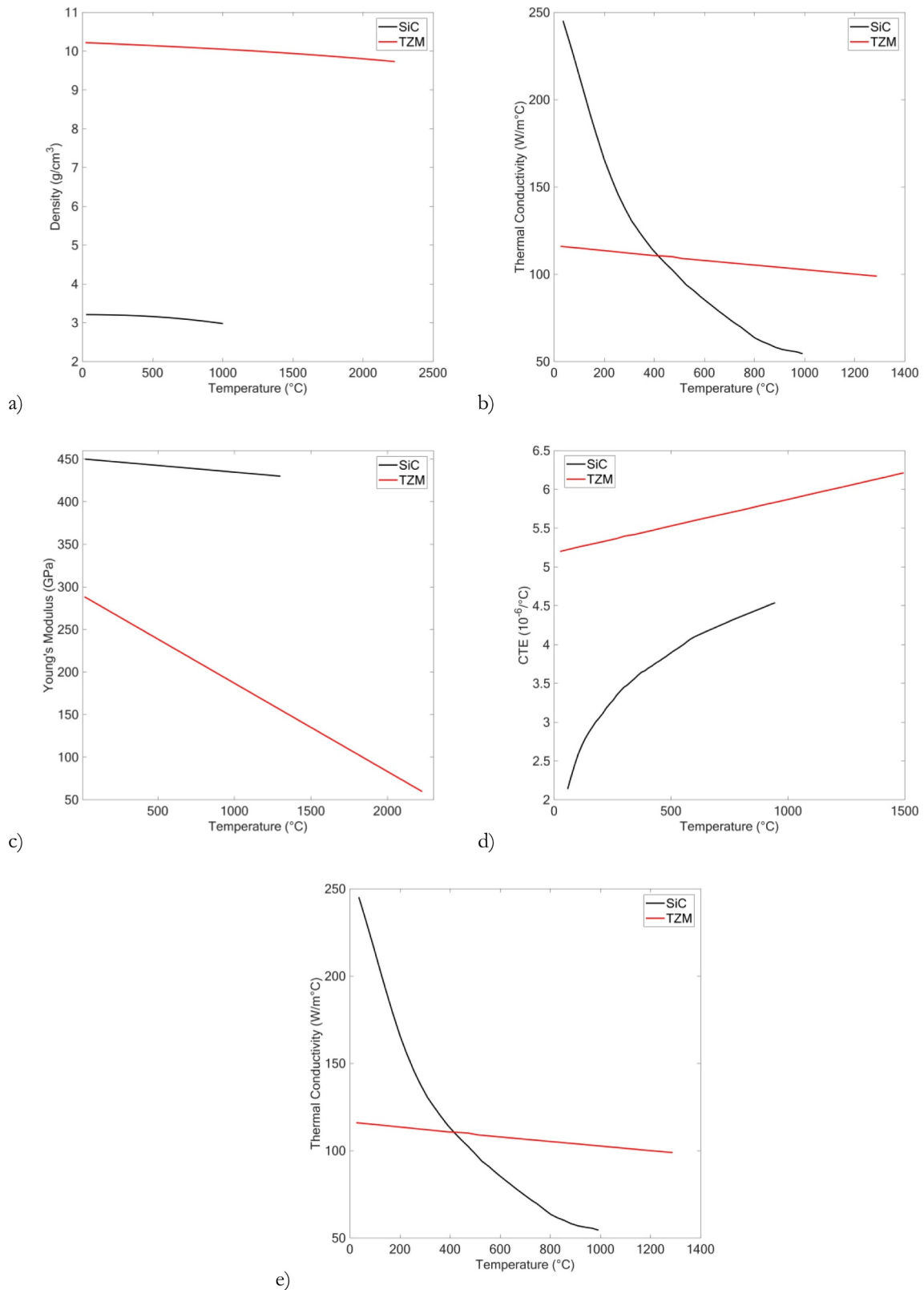
Fig. 2. Temperature-dependent material properties adopted for SiC (black) and TZM (red). The constitutive models adopted also included a constant Poisson's ratio of 0.14 and 0.28 respectively (Microcertec, 2019; Plansee, 2019; Shinno et al., 1988). (For interpretation of the references to colour in this figure legend, the reader is referred to the web version of this article.)

the longitudinal signal.

Following the assumed quasi-instantaneous energy deposition, thermal expansion is initially prevented by the material inertia, establishing a coupling between thermally-induced and inertia forces: in the

case of a slender rod, this results in a compressed state in the heated core, with the stress relaxation initiating from the two extremities of the rod, propagating in the form of stress waves and superimposing at the centre of the rod. The longitudinal frequency of such waves is

Table 1
Bilinear kinematic hardening parameters adopted for TZM and tensile strength values (Shinno et al., 1988) and flexural strength values for SiC as specified by the manufacturer (Microcertec, 2019).

Bilinear kinematic hardening parameters for TZM			
Temperature (°C)	Yield strength (MPa)	Tangent modulus (GPa)	Tensile strength (MPa)
20	764	2.070	965
427	660	2.468	900
829	605	8.780	690

Flexural strength parameters for SiC	
Temperature (°C)	Flexural strength (MPa)
20	450
1300	560

dependent on the speed of sound in the material – a function of its Young's Modulus and density – and the length of the rod, and can be found by Eq. (2):

$$f_L = \frac{c_0}{2L} \qquad (2)$$

where f_L is the longitudinal frequency, L is the length of the rod, $c_0 = \sqrt{E/\rho}$ is the speed of sound, E is the material's Young's Modulus and ρ is the material's density. A reference stress for such waves can be defined by Eq. (3):

$$\sigma_{ref} = E\alpha T_f \qquad (3)$$

where α is the coefficient of thermal expansion of the material and T_f is the final uniform temperature increase of the rod. This stress corresponds to the compressive axial stress induced by a uniform temperature increase T_f in an equivalent rod with fixed ends, and is equal to the maximum stress induced by each stress wave. If the pulse duration is short enough, the maximum dynamic longitudinal stress is thus equal to $2\sigma_{ref}$ when the two waves superimpose.

3.2. Flexural phenomena

In the case of a beam pulse offset in relation to the rod's longitudinal axis, an additional bending response is induced, which is superimposed on the longitudinal signal. The frequency of the first flexural harmonic is a function of the material's Young's Modulus and density, as well as the moment of inertia of the rod's cross-section, the cross-sectional area, the specimen's length, and the boundary conditions, and can be found by Eq. (4):
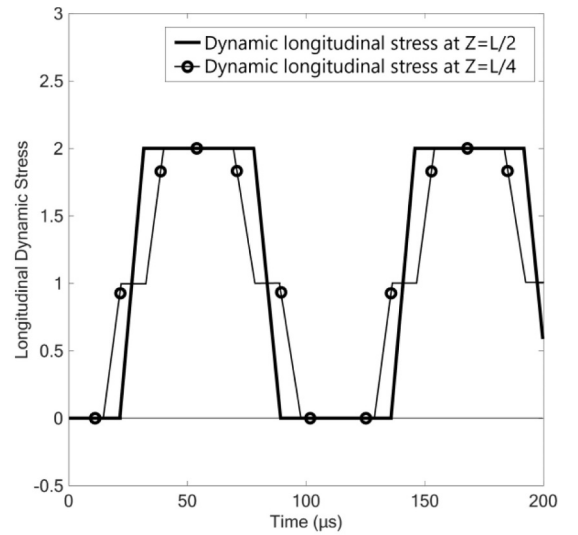
$$f_F = \frac{a^2}{2\pi}\sqrt{\frac{EI}{\rho AL^4}} \qquad (4)$$

where a is a constant dependent on the boundary conditions of the setup, equal to π for a simply-supported configuration and 4.730 for a free-free configuration (Han et al., 1999). As will be seen in experimental results, while the experimental setup consisted of a simply-supported configuration, contact was lost between the specimens and
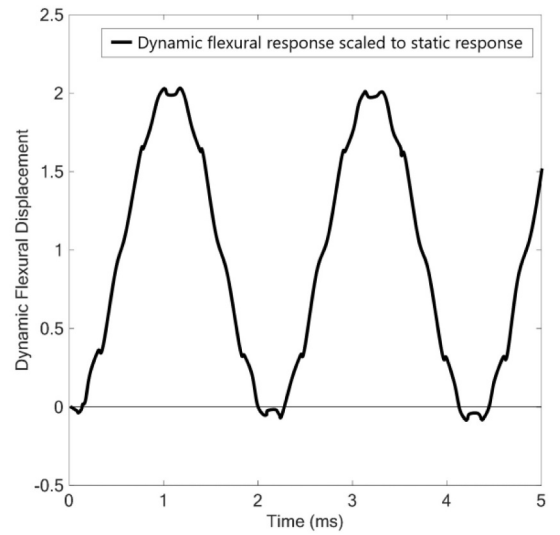
a)

b)

Fig. 3. Longitudinal dynamic stress scaled with the reference stress (a) at the centre of the rod (Z = L/2) and at one-fourth the length of the rod (Z = L/4), and dynamic flexural response at the centre of the rod scaled to the static bending response (b) (Bertarelli et al., 2008).

supports in some cases, resulting in a change in boundary conditions for a period of time. This results in the first few bending oscillations exhibiting a higher frequency corresponding to a free-free condition, with a subsequent gradual transition into a simply-supported condition.

The typical dynamic longitudinal stress plot at a quarter and half the length of the rod scaled to the reference stress, as well as a typical bending stress plot, as computed in Bertarelli's study (Bertarelli et al.,

Table 2
Shots considered in the study of SiC and TZM samples. σ is the transverse beam size and η_y is the vertical offset of the beam considering the defined coordinate system in Fig. 1. Note that the shot 1F is the shot with highest intensity for SiC (being also the final shot for the material). For TZM, the highest intensity shot in the experimental campaign consisted of 36 bunches at a bunch intensity of 1.169×10^{11} protons, a σ of 2 mm and a pulse length of 900 ns (not included in study due to high distortion in experimental readings). Energy stored in one proton (for the beam supplied to the MultiMat experiment) at 440 GeV ($\sim 7.05 \times 10^{-8}$ J).

Shot no.	Material	Pulse Duration (ns)	no. of bunches	Bunch intensity (protons/bunch)	Total intensity (protons)	Total beam energy (J)	Transverse beam size σ (mm)	Vertical offset η_y (mm)	Peak deposited energy (J/m³)
1	SiC	300	12	1.167×10^{11}	1.40×10^{12}	9.87×10^{4}	0.5	4	2.60×10^{8}
1F	SiC	900	36	1.175×10^{11}	4.23×10^{12}	2.98×10^{5}	0.5	0	7.85×10^{8}
2	TZM	600	24	1.100×10^{11}	2.64×10^{12}	1.86×10^{5}	2	-2	2.59×10^{9}
2F	TZM	300	12	1.325×10^{11}	1.59×10^{12}	1.12×10^{5}	0.5	0	6.29×10^{9}

Table 3

First flexural and longitudinal harmonics (analytically calculated through Eqs (2) and (4) with properties at room temperature) for SiC and TZM specimens with length 247 mm and cross-section 10 × 10 mm^2 with simply-supported and free boundary conditions.

	SiC Simply-supported	Free-free	TZM Simply-supported	Free-free
Flexural frequency (Hz)	880	1995	410	930
Longitudinal frequency (Hz)	24,000	11,100		

2008), can be seen in Fig. 3. Note the different time scales for each phenomenon (microseconds for longitudinal wave propagation, and milliseconds for bending oscillations).

Table 3 shows the analytically calculated first longitudinal and flexural harmonics for the SiC and TZM specimens used in the experimental setup, evaluated with material properties at room temperature. As can be seen, when the specimens are in a free condition, the flexural frequency is expected to be more than twice that of when the specimen is in a simply-supported configuration.

4. Numerical modelling of thermally induced stress waves

The experimental scenario was modelled with a weakly coupled thermo-mechanical simulation performed using an implicit finite-element model implementation in ANSYS Workbench 18.1. To model the energy deposition due to the impacting particle beam, energy deposition maps were generated with FLUKA (Ferrari et al., 2005), a Monte-Carlo-based statistical code which outputs the energy deposition for one proton at each mesh element across the specimen volume. This was then imported in ANSYS and scaled accordingly to the total particle intensity of the beam, and is used as an input in the thermal simulation in order to determine the thermal load in each specimen. During impact, a high energy density is induced in high density and high atomic number materials such as TZM, while less energy is deposited in materials having a relatively lower stopping power such as SiC.

The thermal analyses were modelled adiabatically, given that the temperature change in the specimen evolves on a significantly longer timescale (in the order of seconds) when compared to the dynamic phenomena being observed (in the order of microseconds) (Carra, 2017). The thermal analysis consisted of two steps: the first having a duration equal to the energy deposition (i.e. 300 ns for SiC and 600 ns for TZM for shots 1 and 2), and the second having a longer duration to model the temperature evolution in the specimen following the initial temperature increase – in both cases, a load step equal to 3 periods of flexural oscillation was considered. For both modelled impacts, the beam offset is in the vertical X direction, with the beam being symmetrical across the XZ plane, and therefore symmetry on this plane was implemented in both thermal and structural analyses. The mesh size for the thermal analysis was determined to accurately interpolate the energy density map prescribed by FLUKA simulations – in the case of SiC, the mesh consisted of 25 longitudinal divisions, 81 divisions in the X-direction, and 41 divisions in the Y-direction, implementing the coordinate system shown in Fig. 1. Similarly, the model implemented for TZM consisted of 50, 41 and 21 divisions in the Z, X, and Y directions respectively.

Fig. 4 shows the power deposited in each longitudinal division (i.e. along the length of the four specimens) in each station for shots 1 and 2. As can be seen, for SiC (shot 1), the third specimen is the most loaded specimen (left, in yellow), whilst for the TZM station (shot 2) – which, due to the material's high density, absorbs significantly more energy than SiC – the first specimen (right, in blue) is the most loaded. By Eq. (3), the amplitude of the longitudinal wave being studied is a function of the total energy deposited in the specimen, and therefore, when possible, the most loaded specimen for each respective material was considered in this study in order to maximise the signal-to-noise ratio. The thermal analysis results at the end of the energy deposition

showing the temperature along the length of each material station (for shots 1 and 2 respectively) can also be seen in Fig. 4. It is interesting to note that, in the case of SiC, the maximum temperature is actually experienced in the second specimen, however a higher total energy is deposited throughout the third specimen's volume. The longitudinal wave amplitude is a function of the total energy, rather than the peak energy deposition in a specific location. Additionally, a temperature gradient can be observed along the length of various specimens, resulting in longitudinal waves of varying amplitude originating from the rod's extremities – this phenomenon is of particular importance when investigating possible causes of failure of the specimens (Carra, 2017).

The resulting temperature field from the thermal analysis was imported in the structural analysis, which featured three subsequent steps: the first covering the energy deposition and consisting of 10 substeps, the second considering the dynamic longitudinal response, and the third encompassing the dynamic flexural response. The time step for each phase was set accordingly to resolve each phenomenon of interest. The Courant-Friedrichs-Lewy (CFL) condition was adopted to define the required element size for structural analyses, considering the speed of sound in each material, and the respective time step.

5. Benchmarking of numerical and experimental results

The results from the thermo-mechanical simulations were compared against the experimental data acquired from the strain gauges positioned on the specimens, with the final aim of benchmarking the proposed numerical studies, possibly extending the material models currently available in literature. The cut-off frequency considered when importing the experimental data was set to maximise signal-to-noise ratio, considering the frequency of the phenomena of interest, namely flexural, longitudinal and transverse oscillations.

5.1. Longitudinal wave analysis

In Fig. 5, the longitudinal strain response for the third SiC specimen for shot 1 is reported, along with the longitudinal response for the third TZM specimen, for shot two. For both cases, the trapezoidal axial wave shape shown in Fig. 3 is clearly visible in both experimental and numerical results, with a good agreement in longitudinal frequency for SiC and TZM, as can be seen in Table 4. This suggests that the materials' Young's Modulus and density are well replicated in the material models used since, as shown in Eq. (2), the longitudinal frequency is a function of these two material properties (along with the length of the rod). For SiC the wave was heavily distorted by the high noise-to-signal ratio in the experimental signal, given that the longitudinal wave amplitude in this case is an order of magnitude lower than for the most loaded TZM specimen, and therefore further filtering was applied to better distinguish the underlying longitudinal wave.

By Eq. (3), for a given power deposition, slight variations in longitudinal wave amplitude between experimental and numerical results are a function of the Young's Modulus, the coefficient of thermal expansion, and/or the specific heat capacity of the material. For TZM, one can see a frequency difference of 0.6 kHz between analytical and numerical results which can be attributed to the temperature dependency of the material's properties, which are unaccounted for in the analytical model. Given the limited information available from the manufacturer
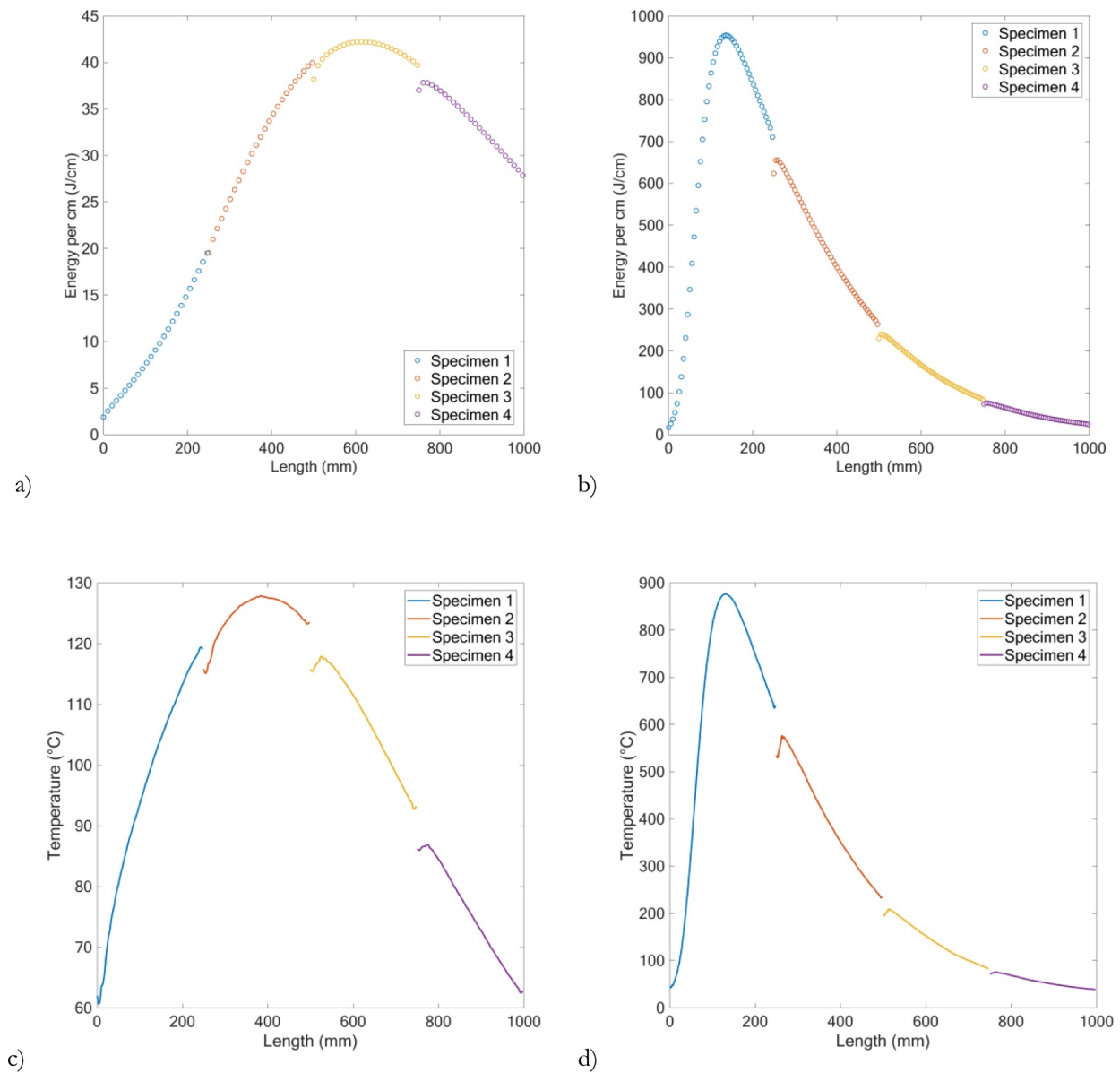
Fig. 4. Power deposited along the length of the each target station for SiC (a) and TZM (b) for the defined pulses, and temperature along the length of target stations for SiC (c) and TZM (d) for shot 1 (at 300 ns) and shot 2 (at 600 ns) respectively. Temperature line along the beam impact position, i.e. at a vertical offset of 4 mm for shot 1 (SiC) and −2 mm for shot 2 (TZM).

for this material, a thermo-mechanical characterisation campaign is to be conducted at CERN facilities to consolidate the available material data. Preliminary impact excitation technique (IET) tests conducted at room temperature resulted in a calculated Young's Modulus of 320 GPa, suggesting an underestimation of the property in the currently available model. It is interesting to note that in the case of TZM, experimental measurements on the second specimen yielded a longitudinal frequency of 14.5 kHz (as opposed to the 11 kHz measured on other specimens), indicating that the specimen had failed upon beam impact or in a previous shot, as will be discussed further on in the section detailing the modelling of specimen failure.

5.2. Bending analysis

Numerical modal analyses carried out prior to the experiment to test the support system implemented indicated that the system behaved in a simply-supported manner, with experimental data matching this assumption in most cases. In some cases, including shots 1 and 2

considered in this study for TZM and SiC, the bending frequency measured in the initial stages of the signal was close to the one expected from a free-free condition. This can be attributed to the impacting beam, which caused some specimens to momentarily lose contact with the supporting structure, resulting in this "free" configuration. This brief loss of contact resulting in the free condition is a result of the supporting spring preload being exceeded once the beam impacts the specimen, resulting in the spring being forced to compress further, and the specimen losing contact with the top graphitic support. This phenomenon is observable in the experimental results for shots 1 and 2, as can be seen in Fig. 6. For SiC, a free condition can be observed in the first 2 ms, before transitioning into a simply-supported configuration. In this case, the time at which the specimen impacts the top support and returns to a simply-supported state is characterised by a sudden jolt in the strain reading at approximately 2 ms, following which a frequency associated with a simply-supported configuration can be observed. Similarly, for TZM, for which the results for the third specimen are presented, the first 5 ms of the signal are characterised by a frequency of
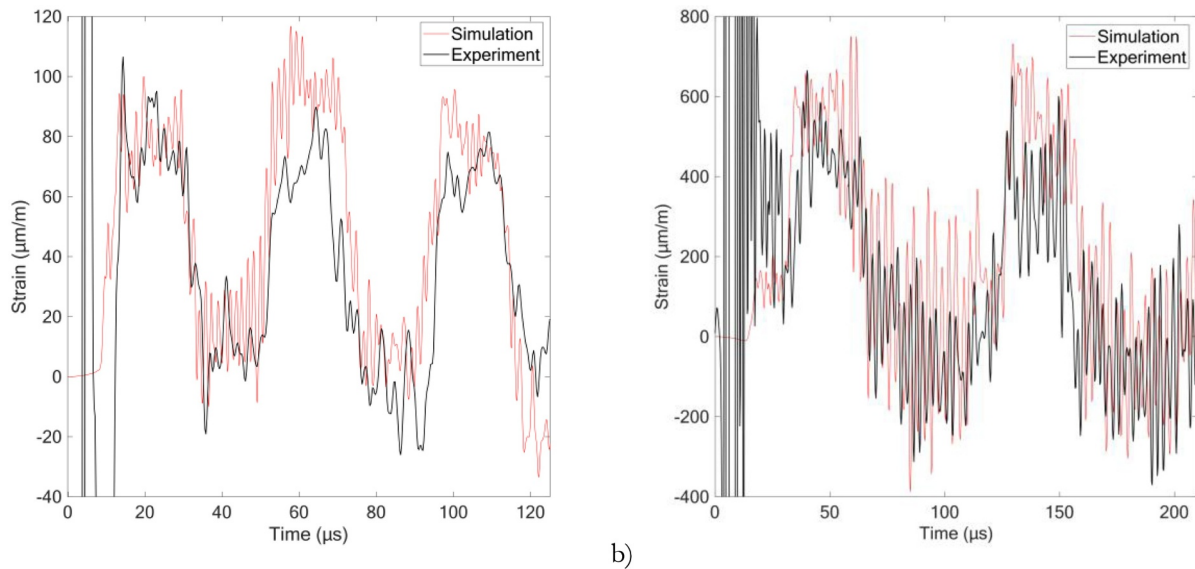
Fig. 5. Experimental and numerical results for axial strain in the third (and most loaded) SiC specimen (a), probed at a length of 106 mm on the bottom face of the specimen, imported with a cut-off frequency of 700 kHz and filtered with a running average over 20 points. Results for the third TZM specimen (b) probed at a length of 165 mm, imported with a cut-off frequency of 600 kHz.

Table 4
Longitudinal wave frequencies from analytical (calculated with Eq. (2)), experimental and numerical results for the third SiC and TZM specimens. Comparable frequencies were recorded in all the other specimens (all having the same dimensions), except for the second TZM specimen, which had broken into two separate pieces as a result of a previous shot.

	Analytical (kHz)	Experimental (kHz)	Numerical (kHz)
SiC	24.0	24.0	23.8
TZM	11.1	11.0	10.5

1050 Hz, corresponding to a free-free condition, before transitioning into a lower frequency corresponding to a simply-supported configuration.

It was deemed important to verify this behaviour by replicating it in a simulation. To this end, two numerical models were implemented in ANSYS. The first model features the "simply-supported" configuration

implemented for the longitudinal wave analysis, which simplifies the experimental setup by restricting vertical movement of the bottom edges at the extremities of each specimen. The second configuration aims to model the experiment's boundary conditions more accurately, particularly the loss of contact between the specimen and the support and the subsequent transition of boundary conditions, implementing compression-only supports at the top of the specimen and a preloaded spring (implementing the same spring characteristics used in the experimental setup, with a spring preload of 13.57 N) at the bottom edge of both extremities. The compression-only support acts as a rigid constraint, thus impeding vertical displacement of the specimens' top edges beyond the support. The specimen can therefore only move in the negative X-direction, resulting in loss of contact with the compression-only support if the reaction force imposed by the spring is exceeded.

Additionally, it is important to note that the simply-supported and free-free conditions considered refer to the vertical motion at the edges of the support and therefore only affect to the bending response of the
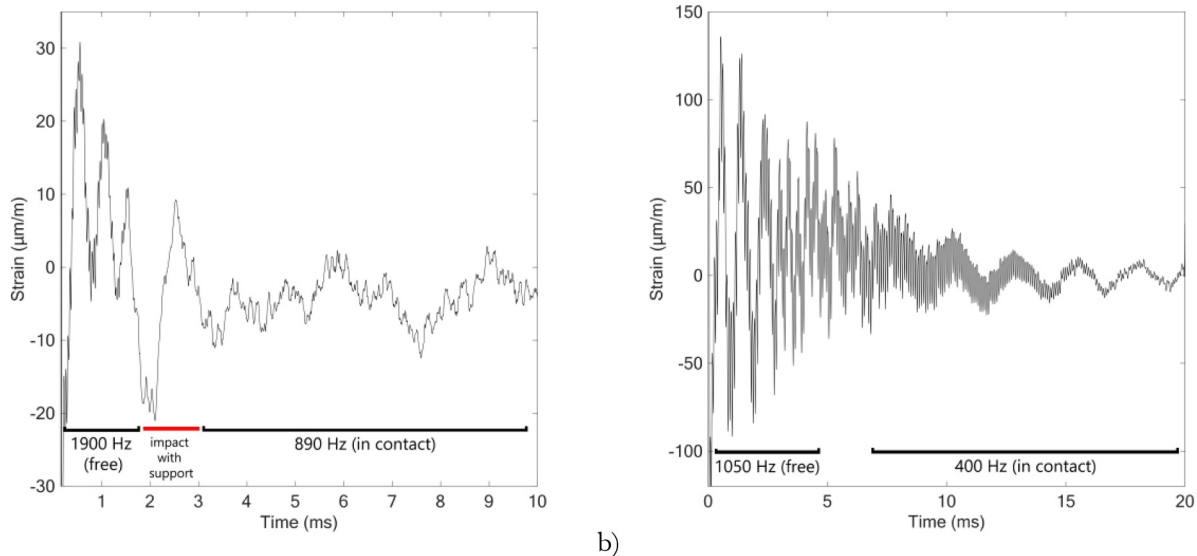

Fig. 6. Experimental results for longitudinal strain exhibiting bending oscillations (superimposed on the longitudinal wave signal) for the third SiC specimen (a), probed at a length of 141 mm on the bottom face of the specimen, and for the third TZM specimen (b), probed at a length of 82 mm.
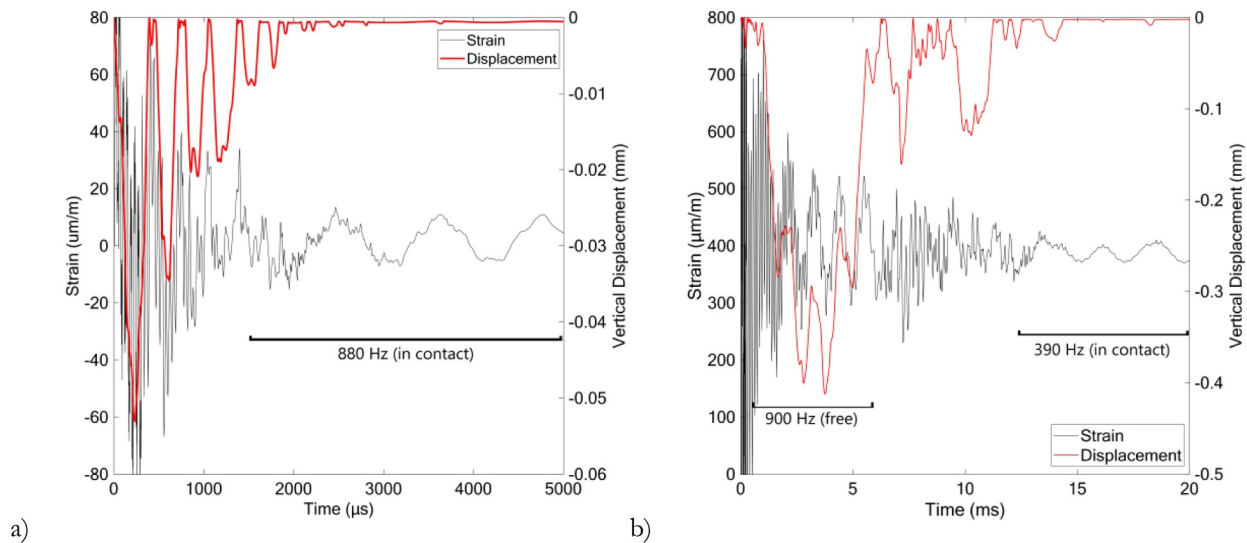
Fig. 7. Numerical results for flexural oscillations (in black) for the third SiC specimen (left) and third TZM specimen (right) with a preloaded spring model of the experimental setup, probed at a length of 141.2 mm and 123.5 mm respectively, with superimposed vertical displacement of top support of specimen (in red). For SiC, a free condition is observed in the first 1 ms of the signal, with a corresponding flexural frequency of 2 kHz and a non-zero vertical displacement, transitioning into a frequency of 880 Hz corresponding to a simply-supported configuration. For TZM, a frequency of 900 Hz is observed in the first 15 ms, corresponding to a free condition, transitioning into a frequency of 390 Hz corresponding to a simply-supported configuration as the vertical displacement converges to zero. (For interpretation of the references to colour in this figure legend, the reader is referred to the web version of this article.)

system. The longitudinal wave propagation is reflected at the free surfaces at the boundaries, which feature in both configurations, and therefore the longitudinal response is identical in both configurations considered. For this reason, in the previous section detailing the longitudinal response, due to the smaller time step required to simulate longitudinal wave propagation, the less computationally intensive option was adopted (i.e. the simply-supported configuration, due to the non-linearity introduced in the spring-loaded model).

Numerical results for the simulations modelling the preloaded spring setup in the experimental scenario for shots 1 and 2 are shown in Fig. 7. For SiC, the first millisecond of the strain signal is characterised by an underlying flexural frequency corresponding to a "free" condition due to the loss of contact between the specimen and the support. This transitions into a frequency of 880 Hz corresponding to a simply-supported configuration. Similarly, for TZM, the signal is initially characterised by a high frequency corresponding to the free state of the specimen, which settles to a frequency of approximately 380 Hz as the specimen settles in position. A summary of frequencies calculated and measured for both configurations can be seen in Table 5.

This change in configuration is better understood when considering the vertical displacement of the top edge of the specimen, shown superimposed in red in Fig. 7. A negative reading corresponds to a loss of contact between the edge and the top support, indicating that the spring preload is exceeded, forcing the spring to compress further. For both materials, it can be seen that contact is lost upon beam impact, and is followed by a transitionary phase where contact is temporarily restored. In both cases, the specimen eventually settles back to its original

(simply-supported) configuration, at which point the vertical displacement of the edge is close to zero.

5.3. Internal damping effects in offset impacts

As observed in Fig. 6, the experimental signal also exhibited damping, which can consist of internal material damping (and can also include external damping). Internal damping effects can be simulated in the numerical model in ANSYS by introducing a stiffness-proportional damping constant $\beta = \zeta/\pi f$, where ζ is the Rayleigh damping ratio and f is the frequency of interest. The logarithmic decrement δ of two successive peaks in the experimental signal was calculated, allowing for the estimation of the damping ratio by $\zeta = 1/\sqrt{1 + (2\pi/\delta)^2}$ (Inman, 2017).

For the results in question, for SiC, damping ratio of $\zeta = 0.08$ was extracted from the logarithmic decay of the experimental bending signal. Similarly, for TZM a damping ratio of $\zeta = 0.05$ was derived from experimental data and implemented in the simply-supported configuration of the analysis, to benchmark the damping response of the experimentally acquired signal characterised by a complete transition to the simply-supported condition at the specimen's boundaries. Fig. 8 shows a comparison of experimental and numerical results following the implementation of damping, with results shown in a time period at which point the experimental setup had settled into a simply-supported configuration (rather than the free condition exhibited in the initial few milliseconds). The damped numerical signal was therefore scaled to the experimental signal's amplitude at this point in time. One should note that the introduction of damping at the bending frequency results in the elimination of higher-frequency components in the simulation, resulting in numerical results having differing characteristics to experimental results (despite the adequate modelling of the average stress value). For centred shots, this method can be similarly implemented on the axial frequencies, where damping can also be observed (having different damping characteristics).

5.4. Benchmarking of failure models

As detailed, both materials experienced failure in a number of specimens. For SiC, failure was observed in the last implemented pulse

Table 5
First flexural frequencies for simply-supported and free-free configurations for SiC and TZM specimens from analytical (calculated with Eq. (4)), experimental, and numerical results (implementing the preloaded spring model).

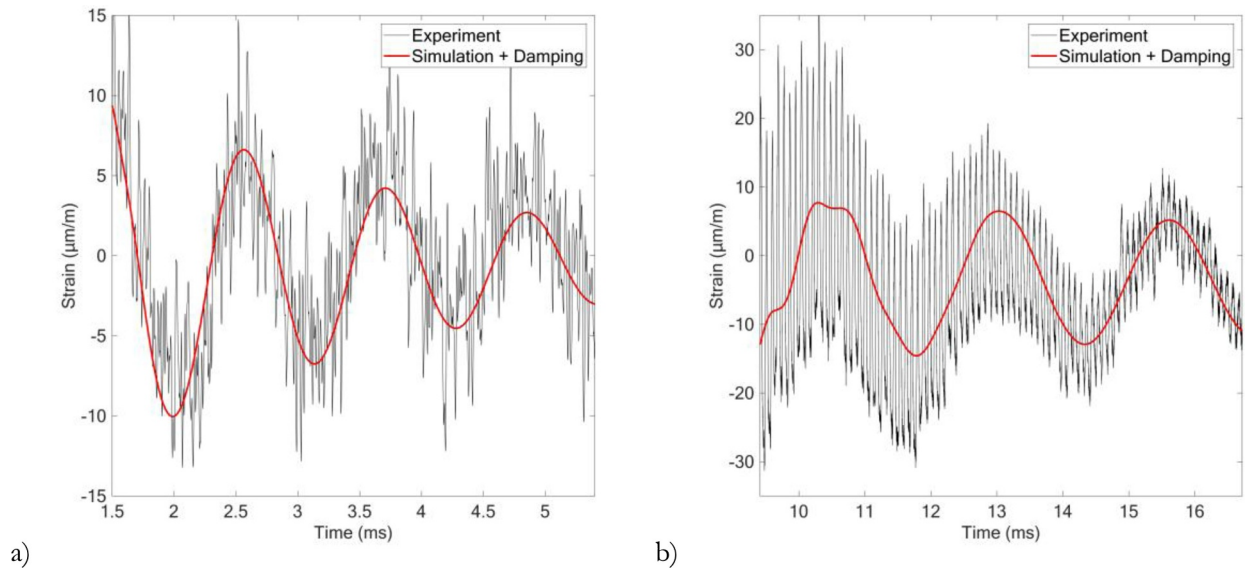|	SiC Simply-supported	Free-free	TZM Simply-supported	Free-free
Analytical (Hz)	880	1995	410	930
Experimental (Hz)	890	1900	400	1050
Numerical (Hz)	880	2000	390	900

Fig. 8. Comparison of experimental and numerical flexural oscillations for the second SiC specimen (a) and the third TZM specimen (b), following the implementation of Rayleigh-damping in ANSYS Workbench, based on the logarithmic decrement obtained from the experimental signal. Strain probed on the bottom face of the specimen at a length of 148 mm and 82.3 mm respectively.
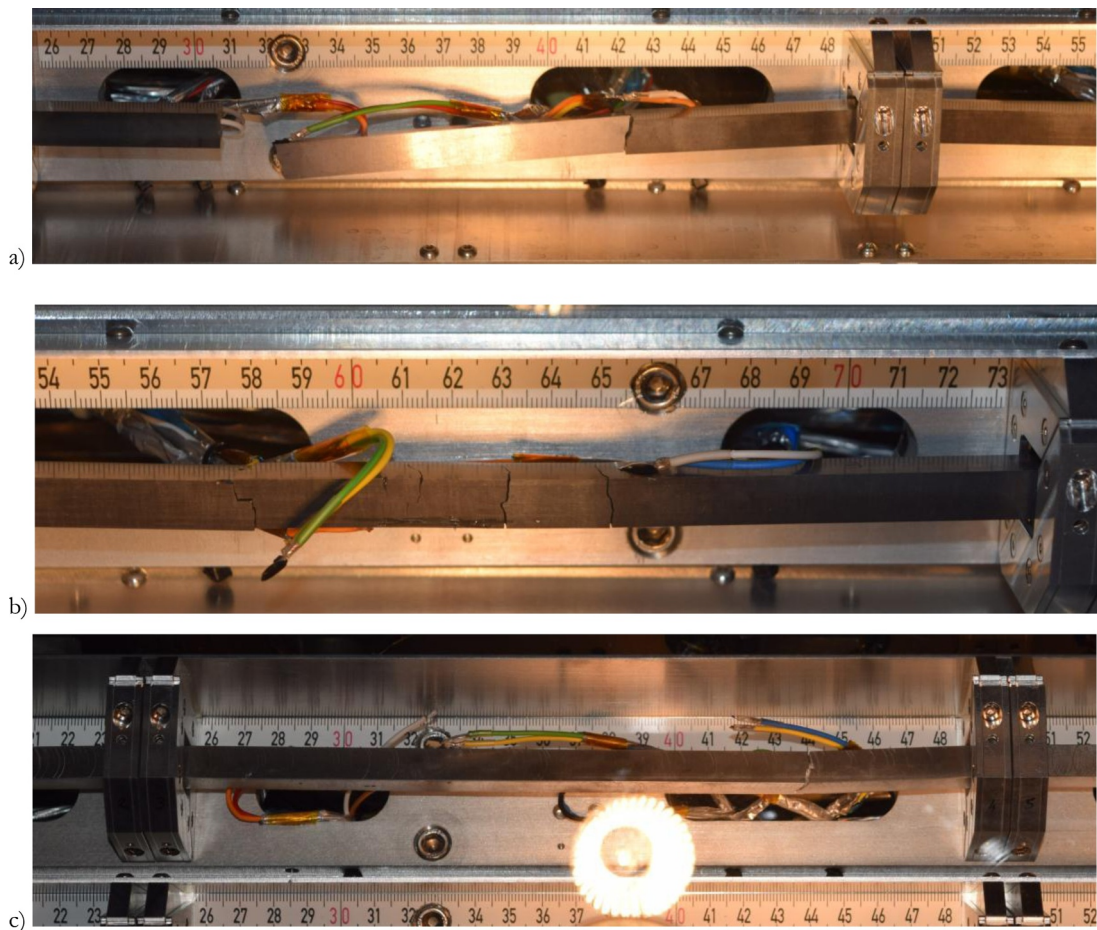

Fig. 9. Fractured SiC specimens, namely specimen 2 ((a), with two cracks at approximately 1/4 and 3/4 of the total length of the specimen) and specimen 3 ((b), with various cracks along its length). Fractured TZM specimen (c) with one crack at a length of approximately 185 mm (3/4 the length of the specimen).

for the material (shot 1F in Table 2), which consisted of a 36-bunch central shot with a pulse length of 900 ns, 1.175×10^{11} protons per bunch, and a beam sigma of 0.5 mm. This resulted in failure in the two most-loaded specimens, namely the second and third specimen, as can be seen in Fig. 9. For TZM, evidence of brittle failure was observed following a pulse consisting of 12 bunches with a bunch intensity of 1.325×10^{11} protons, with a pulse length of 300 ns, a beam sigma of 0.5 mm and no offset (shot 2F in Table 2). The fractured specimen

(specimen 2, also being the second most loaded specimen in the station) can be seen in X-ray tomography tests described in the following section, which also revealed that the first TZM specimen experienced various internal cracks along its length, despite no damage being observed upon the initial visual inspection of its exterior.

Along with the available photos of the broken specimens, evidence of failure can be gathered from experimental strain results. Considering Eqs. (2) and (4), the longitudinal and flexural frequencies being measured are a function of the length of the specimen, and are therefore affected by a specimen breaking in two or more separate pieces. The longitudinal response is especially indicative of the change in length given that, following failure, each part of the specimen has free surfaces at the boundaries which allow for regular longitudinal wave propagation and reflection (and therefore the frequency of the propagating wave can be directly derived from the change in length, provided that the speed of sound remains constant). On the other hand, the flexural response is more complicated to analyse due to the complex boundary conditions in place, with a failure resulting in a free condition at one end of the rod and a dynamically varying condition at the opposing end (due to the preloaded spring setup).

For SiC, failure occurred in two specimens as shown in Fig. 9, with the last pulse for the station (shot 1F). While the third specimen broke at various points along its length, the second specimen can be seen to have fractured in a symmetrical manner, at approximately 1/4th and 3/4th of the specimen's length. The specimen therefore broke into three separate parts, with the two shorter ends having a length of approximately 61.8 mm (i.e. 1/4th the original length) and the middle section having a length of 123.5 mm. The original length has an analytically calculated longitudinal frequency of 24 kHz, and therefore the new lengths result in frequencies of 96 kHz for the shorter parts and 48 kHz for the middle part. The strain gauges were located conveniently on the specimen, with gauges at 49.4, 98.8, 148.2 and 197.6 mm, i.e. one gauge on each of the shorter ends of the specimen, and two gauges on the middle section.

The failure of the specimens was modelled in ANSYS Workbench by using the element birth and death functions. The program gives the option to perform element birth and death between load steps, thus allowing for the elimination of certain elements or contact points based on element results (such as equivalent stress, strain etc.) or load step number. This feature can be used to model the failure of an object once a maximum limiting value is reached or at a specific moment in time. The element death function was implemented in ANSYS and used to "kill" two slices of elements at lengths of 61.8 mm and 185.3 mm at the time of failure (corresponding to the two points of fracture observed in post-irradiation photos, as seen in Fig. 9 for specimen 2). Another approach is to slice the geometry into three separate sections (two having a length of 61.8 mm and the middle section having a length of 123.5 mm), and apply a bonded contact between the different parts, which is subsequently eliminated at the time of failure. Both methods were tested (element and contact killing), achieving comparable results.

Fig. 10 shows the experimental result for the gauge at a length of 98.8 mm, plotted with the numerical results implementing element killing at 20 μs. The experimental signal can be seen to distort at the 20 μs, following which a signal frequency of approximately 47 kHz can be observed, corresponding to a specimen having half the original specimen length. The simulation can be seen to replicate the new longitudinal frequency adequately (corresponding to the new length following failure at 20 μs) with a frequency of 47.5 kHz. The two results can be seen to differ in terms of amplitude, with the simulation retaining the original wave amplitude and not accounting to loss of energy as a result of the failure.

For shot 1F, simulation results for specimen 2 indicated temperatures ranging from room temperature up to 316 °C. At the observed maximum temperature, flexural strength values for the material are in the order of 475 MPa (assuming a linear fit between the two provided data points), while equivalent stress values up to 480 MPa can be
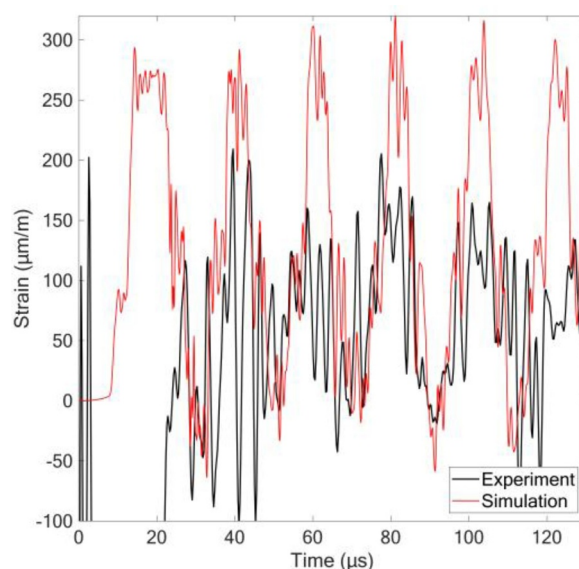

Fig. 10. Comparison of experimental results from the strain gauge at 98.8 mm for SiC specimen 2 with numerical model simulating failure at 20 μs.

observed in structural analyses. One should note that flexural strength values available were obtained through static 4-point bending tests, while relatively high strain rates can be observed in experimental results (in the order of 500 s^{-1}).

As discussed, the symmetrical failure of the specimen indicates that this was caused by the passing of the two longitudinal waves originating from each extremity of the rod. Simulation results indicate that each respective longitudinal wave reaches its maximum amplitude before reaching the points of failure (at ¼ the length of the rod from each extremity), and therefore it has proven challenging to characterise the reason for the specimen to fail at these specific positions (rather than at an earlier point).

In the case of TZM, the change in longitudinal frequency can be seen in the shots causing the failure of the specimen (shot 2F) as well as in later shots (including shot 2 as previously discussed). Similar to the results observed in SiC, a higher longitudinal frequency (compared to the one measured in the other [intact] specimens, i.e. retaining the original length of 247 mm) is measured in different parts of the broken specimen, corresponding to the new respective length of each part following failure. The specimen can be seen to have fractured at a length of approximately 185 mm, resulting in two parts: one having a length of 185 mm and another having a length of 62 mm. Strain gauges on each separate piece of the specimen should therefore measure a longitudinal frequency of 14.5 kHz and 45 kHz respectively, by Eq. (2). This can be seen in Fig. 11, which shows the experimentally acquired longitudinal strain signal for the second TZM specimen for shot 2F. Results are shown for two longitudinal strain gauges, gauges 3 and 4, positioned on the bottom face of the specimen at longitudinal lengths of 148 mm and 198 mm respectively, meaning that they were positioned on opposite sides of the point of failure. One should note that for the specimen in question there is a temperature gradient along its length, resulting in the longitudinal waves propagating from each extremity of the rod having differing amplitudes. The right half of the rod (i.e. closer to gauge 4) has less energy deposited and therefore the wave originating from this extremity has a lower amplitude compared to that originating from the left end of the specimen.

The longitudinal wave period for the rod with original length of 247 mm (as can be seen in results for unbroken specimens) is approximately 90 μs. As can be seen by the change in frequency in Fig. 11, the specimen breaks well before the longitudinal wave propagates through the specimen and is reflected back to its original position. The
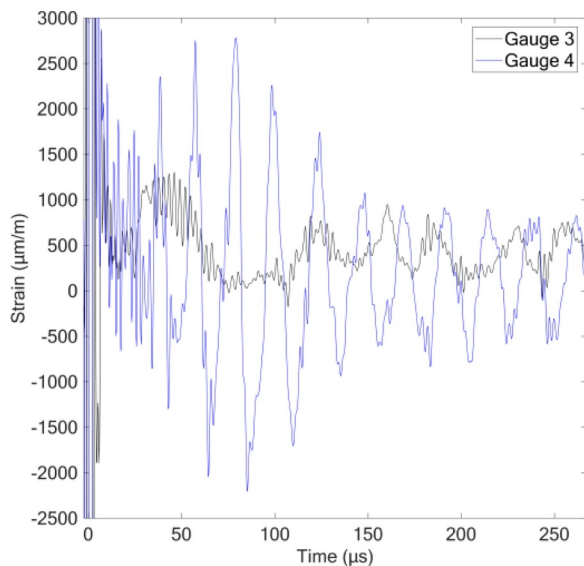
Fig. 11. Experimental results for the second TZM specimen for shot 2F. Note that gauge 3 is located at a length of 148 mm (left-hand side of the point of failure) and gauge 4 is located at a length of 198 mm (right-hand side of point of failure).

position of the fracture is at a length of approximately 185 mm, whilst the speed of sound in TZM is approximately 5500 m/s. Following the particle beam impact, the wave with smaller amplitude propagating from the edge closest to the fracture location (i.e. the right-hand side) takes 11 μs to traverse 62 mm and reach the point of eventual failure, whilst the higher-amplitude wave propagating from the left-hand side takes 34 μs to reach the same point. As can be seen in Fig. 11, the high-frequency wave detected by the 4th strain gauge (a result of the new length of 62 mm for this part of the specimen, following failure) has a relatively high amplitude compared to the wave detected by the third gauge.

Element death function was again implemented in ANSYS and used to "kill" a slice of elements at a length of 185 mm at the time of failure. Using this approach, two scenarios were considered – one where the specimen fractures at 11 μs (with the arrival of the lower-amplitude right-hand wave), and one where the specimen fractures 45 μs into the simulation (following the passing of the higher-amplitude left-hand wave). The results for these two scenarios, for the strain gauges positioned at a length of 148 mm and 198 mm, can be seen in Fig. 12 (top). In the first case, with failure at 11 μs, the high-amplitude wave travelling from the left-hand side never reaches gauge 4, due to the specimen breaking before this wave reaches the point of failure. One can see that the results displayed in Fig. 12 (top, left) feature a very small amplitude measured by gauge 4, differing from the experimental scenario shown in Fig. 11. In Fig. 12 (top, right), results from the analysis modelling failure at 45 μs are shown. For the first 45 μs, the results are identical to a simulation where no failure is simulated (since failure is implemented in the analysis at 45 μs). One can clearly see the lower-amplitude longitudinal wave coming from the right end of the sample reaching the gauge 4 at approximately 11 μs (blue plot), before the maximum amplitude is reached once the higher-amplitude longitudinal wave (coming from the left end) reaches this location, and the two waves superimpose. Failure is simulated at 45 μs, resulting in the two gauges measuring distinctly different frequencies, dependent on the length of each respective broken part of the specimen (14.5 kHz for gauge 3 and 45 kHz for gauge 4). The simulation results probed at gauge 4 for this scenario are more comparable to experimental results than in the case with failure at 11 μs, suggesting that the specimen fails due to the arrival of the higher-amplitude wave from the left-hand side, with some of the energy from this wave still being transferred to the

right-hand side of the specimen, which is subsequently "trapped" in this region, resulting in the high-amplitude signal seen in both simulation and experimental results at gauge 4. This hypothesis suggests that the cause of failure of this specimen could have been a defect or void in the sample, which exhibits failure only on the arrival of the higher-amplitude stress wave (propagating from the left-hand side of the specimen).

As discussed, this specimen – which is the second most loaded in terms of thermal load – failed, while the most loaded specimen remained intact. For shot 2F, simulation results indicate temperatures up to 400 °C in the core of the most loaded specimen, whilst for the failed specimen the maximum temperature is 362 °C on the point of failure, reducing to a maximum of approximately 200 °C at the point of failure. A cause for the failure of the second most loaded specimen (as opposed to the most loaded one) could therefore be the higher brittleness of the specimen due to its lower temperature, a result of TZM's ductile-to-brittle transition temperature (DBTT). In a study by Hiraoka et al investigating the ductile-to-brittle transition characteristics of Molybdenum and its alloys, including TZM, the DBTT in impact tests was found to be higher than that in static tests, indicating that a lower loading rate could result in a brittle failure at lower temperatures (Hiraoka et al., 1995). As detailed, a post-irradiation examination consisting of computed tomography imaging was conducted in the CERN laboratories to assess the condition of the specimens, with particular focus on the failed specimens.

Fig. 12. (bottom) summarises the propagation of the waves originating from each end of the rod, and how each wave is affected by the failure of the TZM specimen. The top figure shows the position of each wave-front at 11 μs, at which point the wave propagating from the right-hand side reaches the eventual point of failure. The middle diagram shows the position of the two waves at 34 μs, at which point the wave travelling from the left-hand side – having a larger amplitude – reaches the length of 185 mm and causes the specimen to fail. The final diagram indicates that some of the wave's energy is transferred to the right-hand side of the specimen, which subsequently separates from the rest of the specimen, while some of the energy is reflected back at the newly-formed boundary. The position of the two strain gauges at 148 mm and 198 mm are marked in black and blue respectively.

The bilinear kinematic constitutive law for TZM implemented in the numerical model modelling the MultiMat experiment indicates stress levels in the order of 900 MPa, exceeding non-dynamic yield and ultimate tensile strength values specified for TZM by the manufacturer. While the quasi-static strength is exceeded in both first and second TZM specimens, only the second specimen exhibited failure in the experiment, suggesting that the material model requires further refinement to include strain rate and temperature dependency. The strain rate observed in experimental results is in the order of 1000 s^{-1}, at which point the material behaviour might differ significantly from steady-state conditions. While information on the material behaviour at such strain rates is not provided by the manufacturer, literature investigating the mechanical modelling of pure molybdenum at strain rates and temperatures in this order of magnitude is available, detailing the mechanical response of the material across a wide range of temperatures and strain rates, including the types of failure observed (Scapin et al., 2016, 2015). Lacking any other means of comparison, the information available on Mo was taken as a qualitative reference, keeping in mind that the two materials can exhibit substantial differences in high-strain rate behaviour despite the small differences in composition. Results for pure Mo indicate that brittle failure is observed at high strain rates and low temperatures (Scapin et al., 2016), which is also the type of failure observed in the MultiMat experiment for TZM, indicating that the material could be in a range of temperature and strain rate compatible with brittle failure. In addition to quasi-static tests, additional tests are therefore required in order to accurately model the material behaviour across a wide range of impact scenarios. The experimental campaign will consist of direct Hopkinson Bar setup, allowing the investigation of the mechanical behaviour in varying strain
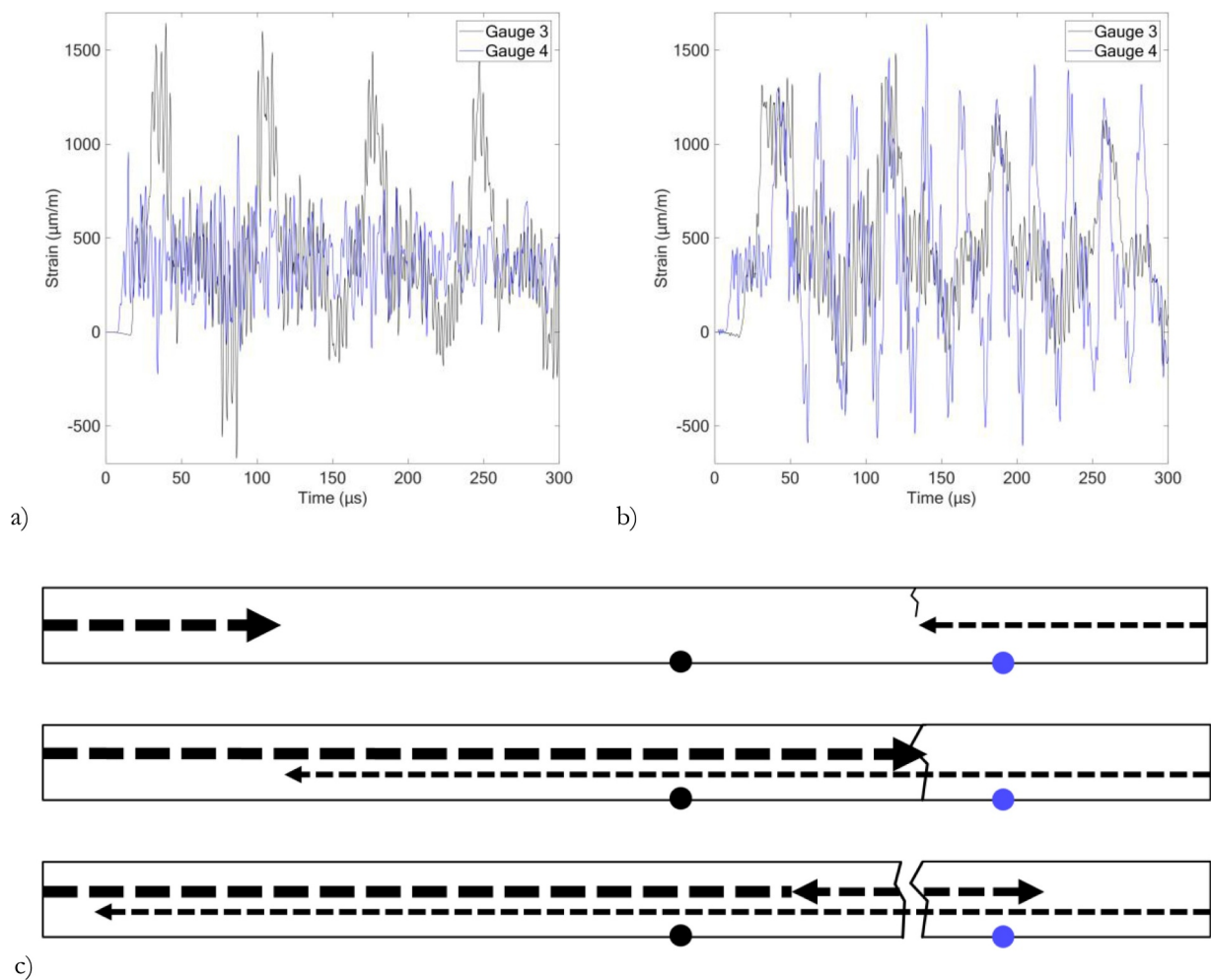
Fig. 12. Numerical results for the second TZM specimen (top) for shot 2F, with element killing at 11 μs at the point of failure (a), and for element killing at 45 μs at the point of failure (b). Bottom diagram (c) shows the left and right-hand side wave propagation along the specimen's length and its subsequent failure on the arrival of the higher amplitude wave from the left-hand side, i.e. following the hypothesis of fracture at 45 μs as per top right results.

rates and temperatures.

6. Post-irradiation X-ray tomography campaign

Initial visual inspections on TZM specimens following the experimental campaign only showed damage on the second most loaded specimen, as discussed. Following the completion of the experiment, the test-bench was transferred to a storage area and was opened once the dose rate reduced to safe levels in early 2019. A post-irradiation X-ray tomography campaign was subsequently conducted on various specimens, revealing that the most loaded TZM, which, given the failure in the second most loaded specimen, was also expected to fail, does in fact exhibit a number of internal cracks. As can be seen in Fig. 13, a long crack is clearly visible along the whole length of the specimen, along with various cracks across the cross-section. Images from the scans on the second TZM specimen clearly show the point of failure, while a top view of the most loaded SiC specimen allows a clear view of the various cracks near the centre of the sample.

7. Conclusions

The MultiMat experiment was conducted in the HiRadMat facility at CERN in the end of 2017, with the aim to explore previously unknown material properties of materials used in beam intercepting devices. Material constitutive models, required to simulate dynamic phenomena generated by particle beam impacts, are not widely available in literature, and therefore dedicating testing such as that performed in the HiRadMat facility is required to explore material states which are not attainable with standard testing methods.

This study focuses on the results generated for two materials, namely Silicon Carbide and Titanium Zirconium Molybdenum, benchmarking the currently available material models with experimental data. The analysis focuses on the longitudinal and flexural dynamic phenomena observable following the particle beam impact, discussing factors such as frequency and amplitude of the observed oscillations, material damping, and boundary-condition effects on the generated signal. In addition, a discussion on the eventual failure of certain specimens is presented, detailing possible causes of failure. Studying such phenomena allows for the benchmarking of the material models, which need to be able to model the material's thermal and mechanical behaviour across a wide range of scenarios.

The study simulated the experimental setup by implementing a simply-coupled thermo-mechanical analysis in ANSYS Workbench. The thermal analysis modelled the energy deposition in the material specimens, with the resulting temperature field imported in structural analyses to model the dynamic response of the system. The longitudinal response was initially modelled, with the presented experimental results matching well with computational results in terms of wave shape, frequency and amplitude. The bending response of the specimens was similarly modelled. In this case, attempts were made to simulate the exact boundary conditions of the experimental setup, which consisted of graphitic supports kept in position by a preloaded spring. This
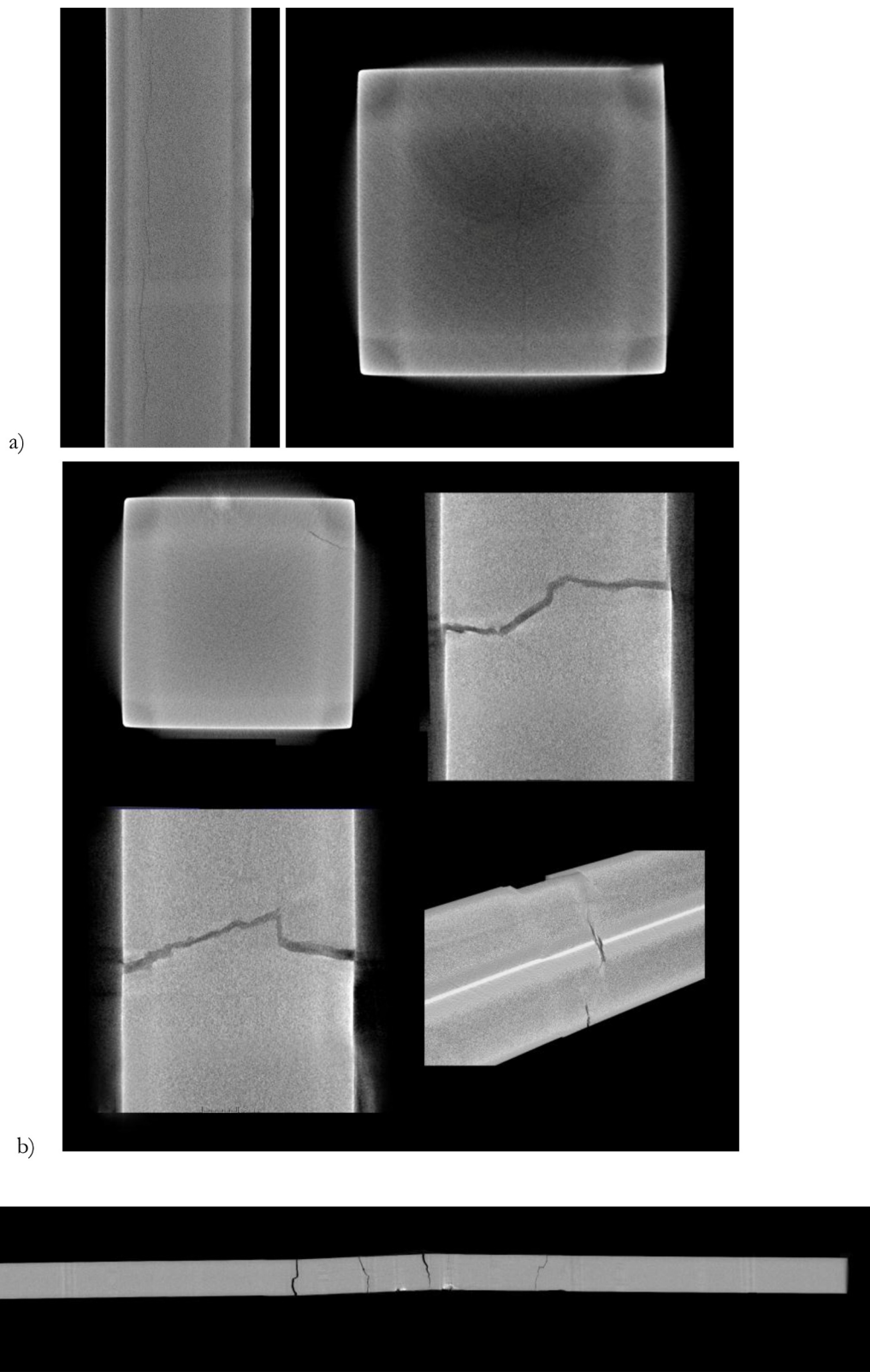
Fig. 13. X-ray tomography scans of the most loaded TZM specimen (a), showing a crack along its length (left) and various cracks across its cross-section (right), of the second most loaded TZM specimen (b), showing the point of failure from various angles, and the most loaded SiC specimen (c), showing various cracks near the centre of the sample.

resulted in a change of boundary conditions upon beam impact, due to a brief loss of contact between the specimens and the support, which could be observed as a change in frequency in the flexural response. The boundary conditions were modelled in ANSYS, successfully simulating the loss of contact, and subsequent transition in flexural frequencies. The damping observed in the experimental signal was also successfully modelled through the application of Rayleigh damping in ANSYS Workbench.

Table 6

Summary of material properties at room temperature.

Property at room temperature (20 °C)	SiC	TZM
Young's modulus (GPa)	450	288
Thermal conductivity (W/m°C)	240	116
CTE (10^{-6}/°C)	1.8	5.2
Density (kg/m³)	3210	10,220
Specific heat capacity (J/kg°C)	708	272
Strength (MPa)	450 (Flexural strength)	965 (UTS)

Finally, the failure in various specimens was discussed and modelled. Element birth and death functions were applied in ANSYS in order to simulate the failure of TZM and SiC specimens due to the propagating longitudinal wave. As observed in experimental results, this resulted in a range of measured longitudinal frequencies, dependent on the length of each respective part of the specimen following failure. The symmetrical nature of failure in SiC specimens suggests that this is caused by the passing of the two longitudinal waves originating from the extremities of the specimen, however it is not yet understood why the specimen specifically fractured at a quarter length from each respective side. A post-irradiation X-ray tomography campaign aided in identifying various cracks along the length and cross-section of the most loaded TZM specimen, which was previously believed to have remained intact following the experimental campaign.

The material models implemented, a summary of which is shown in Table 6, using a combination of properties provided by the respective manufacturers and literature, proved to be sufficient to successfully model a number of experimental scenarios considered. Strength data available was compared with stress results computed in numerical analyses, which indicated that the specified values had been exceeded with the material models implemented. A post-mortem analysis consisting of X-ray microtomography measurements has been conducted on a number of material samples which experienced failure during the experiment, allowing for additional observation of internal crack propagation within the specimens which had been previously undetected with visual inspection. For both materials, further metrology measurements and thermo-mechanical testing is expected to be conducted at CERN to verify the data obtained from literature. This includes Impact Excitation Technique tests, which are to be conducted across a range of temperatures, allowing the calculation of elastic properties, as well as testing for the calculation of specific heat capacity, coefficient of thermal expansion, density, and conductivity of the materials.

The main limitation of the currently available models was found to be the lack of inclusion of strain rate effects on the mechanical properties of the two materials. The adoption of equations of state, strength and failure models is required to accurately model the full material behaviour across a wide range of pressures, strain rates, temperatures, and geometries commonly encountered in particle beam impact scenarios. In this regard, Hopkinson bar tests are scheduled to be conducted to complement the quasi-static material characterisation and complement the currently available material models.

The main conclusions of the study are summarised below:

- The currently available material models for the Silicon Carbide and Titanium Zirconium Molybdenum grades tested in the MultiMat experiment successfully replicated longitudinal and flexural phenomena when implemented in implicit numerical simulations in ANSYS Workbench.
- The complex boundary conditions present in the experiment were also successfully modelled, allowing for the simulation of the transition from a "free" to a "simply-supported" condition, as observed in experimental results.
- Further experimental testing is required to fully model the material behaviour at high strain rates and temperatures, along with failure scenarios.

References

ANSYS, Inc., 'Ansys Autodyn User's Manual - Release 15.0', 2013.

ANSYS, Inc., 'Ansys Mechanical User's Manual - Release 15.0', 2013.

Apollinari, G., et al., 2017. High-Luminosity Large Hadron Collider (HL-LHC). High-Luminosity Large Hadron Collider (HL-LHC) 4 CERN, Geneva Technical Design Report.

Bargmann, H., 'Dynamic Response of External Targets Under Thermal Shock', CERN Technical Note No. LAB II/BT/Int/73-3, 1973.

Benedikt, M., Zimmerman, M., 2016. Future circular colliders. Proc. Int. Sch. Phys. Fermi 194, 73–80.

Bertarelli, A., et al., 2006. Permanent Deformation of the LHC Collimator Jaws Induced by Shock Beam Impact: an Analytical and Numerical Interpretation. pp. 3.

Bertarelli, A., et al., 2012. High Energy Tests of Advanced Materials for Beam Intercepting Devices at CERN HiRadMat Facility. pp. 5.

Bertarelli, A., et al., 2013. Behaviour of advanced materials impacted by high energy particle beams. J. Phys. 451 (1), 012005.

Bertarelli, A., et al., 2015. Innovative MoC – graphite composite for thermal management and thermal shock applications. In: Presented at the 2015 31st Thermal Measurement, Modeling Management Symposium (SEMI-THERM), pp. 56–59.

Bertarelli, A., 2016. Beam-Induced Damage Mechanisms and their Calculation. CERN 0007–8328.

Bertarelli, A., Arnau Izquierdo, G., Carra, F., Dallocchio, A., Gil Costa, M., Mariani, N., 2011. Research and development of novel advanced materials for next-generation collimators. In: Presented at the 2nd International Particle Accelerator Conference. San Sebastian, Spain.

Bertarelli, A., et al., 2013. An experiment to test advanced materials impacted by intense proton pulses at CERN HiRadMat facility. Nucl. Instrum. Methods Phys. Res. Sect. B 308 (Aug.), 88–99.

Bertarelli, A., Carra, F., Mariani, N., Bizzaro, S., 2014. Development and Testing of Novel Advanced Materials with Very High Thermal Shock Resistance. EuCARD-2 Scientific Report CERN-ACC-2014-0306.

Bertarelli, A., Dallocchio, A., Kurtyka, T., 2008. Dynamic response of rapidly heated cylindrical rods: longitudinal and flexural behavior. J. Appl. Mech. 75 (Apr. (3)), 031010.

Carra, F., et al., 2014. Mechanical engineering and design of novel collimators for HL-LHC. In: IPAC.

Carra, F., 2017. Thermomechanical response of advanced materials under quasi instantaneous heating. Ph.D. thesis, Politecnico di Torino, Italy, pp. 110–119. https://zenodo.org/record/3237544#.XW5Q7igzbD4.

Carra, F., et al., 2017. The "Multimat" experiment at CERN HiRadMat facility: advanced testing of novel materials and instrumentation for HL-LHC collimators. In: Journal of Physics: Conference Series. Copenhagen, Denmark. 874.

Cauchi, M., et al., 2014. High energy beam impact tests on a LHC tertiary collimator at the CERN high-radiation to materials facility. Phys. Rev. ST Accel. Beams 17 (Feb. (2)), 021004.

Efthymiopoulos, I., et al., 2011. HiRadMat: A New Irradiation Facility for Material Testing at CERN. In: presented at the 2nd International Particle Accelerator Conference (IPAC 2011). San Sebastián, Spain. pp. 1665–1667.

Ferrari, A., Sala, P.R., Fassò, A., Ranft, J., 2005. FLUKA: A multi-particle transport code (program version 2005). CERN, Geneva.

Graff, K.F., 1991. Wave Motion in Elastic Solids, New York. pp. 116–121. Dover Publications Inc.

Han, S.M., Benaroya, H., Wei, T., 1999. Dynamics of Transversely vibrating beams using four engineering theories. J. Sound Vib. 225 (Sep. (5)), 935–988.

Hiraoka, Y., Kurishita, H., Narui, M., Kayano, H., 1995. Fracture and ductile-to-brittle transition characteristics of molybdenum by impact and static bend tests. Mater. Trans. JIM 36 (4), 504–510.

Inman, D.J., 2017. Engineering Vibration, third ed. Prentice Hall PTR, Upper Saddle, New Jersey, pp. 43–48.

Microcertec, 'Matériaux : Carbure de Silicium (SiC)' 2019. [Online]. Available: http://www.microcertec.com/fiche-materiaux-fr-9-carbure-de-silicium-sic.html.

Pasquali, M., et al., 2019. Dynamic response of advanced materials impacted by particle beams: the MultiMat experiment. J. Dyn. Behav. Mater. 5 (3), 266–295.

Plansee, 'Molybdenum'.2019[Online]. Available:https://www.plansee.com/en/materials/molybdenum.html.

Portelli, M., Bertarelli, A., Carra, F., Mettler, L.K., Mollicone, P., Sammut, N., 2018. Numerical simulation of long rods impacted by particle beams. Phys. Rev. Accel. Beams 21 (Jun. (6)).

Quaranta, E., 2017. Investigation of Collimator Materials for the High Luminosity Large Hadron Collider. Politecnico di Milano, Italy.

Scapin, M., Fichera, C., Carra, F., Peroni, L., 2015. Experimental investigation of the behaviour of tungsten and molybdenum alloys at high strain rate and temperature. In: EPJ Web of Conferences. 94. pp. 01021.

Scapin, M., Peroni, L., Carra, F., 2016. Investigation and mechanical modelling of pure molybdenum at high strain rate and temperature. J. Dyn. Behav. Mater. 2 (Dec. (4)), 460–475.

Shinno, H., Kitajima, M., Okada, M., 1988. Thermal stress analysis of high heat flux materials. J. Nucl. Mater. 155–157, 290–294.

Sievers, P., 'Elastic Stress Waves in Matter Due to Rapid Heating by an Intense High-Energy Particle Beam', CERN Technical Note No. LAB II/BT/74-2, 1974.